Available online at www.sciencedirect.com
ScienceDirect
Journal of Crystal Growth 295 (2006) 188–201
JOURNAL OF CRYSTAL GROWTH
www.elsevier.com/locate/jcrysgro

Morphological instability during directional epitaxy

Tim P. Schulze

University of Tennessee, 121 Ayres Hall, Knoxville, TN 37996 1300, USA

Received 2 December 2005; received in revised form 14 July 2006; accepted 26 July 2006
Communicated by G.B. McFadden

Abstract

We consider the stability of a single step during epitaxial growth of a monolayer on a continuously supplied substrate in the presence of an imposed gradient in the deposition rate along the direction of growth. This allows control of instabilities that arise from asymmetries in the supply of atoms attaching from the upper and lower side of the step. We consider both a linear stability analysis of a mean-field terrace-step model and kinetic Monte-Carlo (KMC) simulation of an atomistic growth model.

Keywords: A1. Epitaxial growth; A1. Kinetic Monte-Carlo; A1. Morphological instability

1. Introduction

Epitaxial growth is widely recognized as an important technological process at the center of the quest for ever smaller electronic devices. The ability to create specific patterns on surfaces is essential to this purpose and particular attention has been paid to systems with naturally forming patterns that could be exploited. It is well known that a uniformly propagating train of steps is subject to a meandering instability if the atoms attaching to the growing front arrive preferentially from the direction in which the steps are propagating [1]. In many systems, there is a natural tendency for this to happen due to step-edge barriers that somewhat inhibit atoms arriving from the upper terrace from attaching to a step [2–4]. The aim of this paper is to explore the active control of these instabilities by a nonuniform deposition process applied to a continuously supplied substrate.

For the most part, we shall focus on the stability of a single step during monolayer growth on the surface of a wire or tape fed at constant speed V into a deposition zone (Fig. 1). This scenario admits a steady state with uniformly propagating front analogous to the "directional solidification" scenario that is much studied in the bulk crystal growth literature [5]. We therefore refer to this as "directional epitaxy". Within the epitaxy literature this type of processing, not necessarily restricted to monolayer growth, is often referred to as "reel-to-reel" and has been of particular interest for producing large quantities of superconductor-coated wires or tapes [6]. While we limit the present study to single species growth, the patterns that emerge may provide a practical means of constructing self-assembled monolayers during the growth of multispecies films.

There are two major differences between this situation and previous analysis [1,7–9] of the mean-field terrace-step model introduced by Burton et al. (BCF) [10] or previous simulations using kinetic Monte-Carlo simulations [11,12]: (i) since we consider deposition onto a continuously supplied substrate, the helical boundary conditions (described below) that have typically been implemented in the direction of growth are no longer appropriate, and (ii) since the mean position of the step will be steady in the laboratory frame of reference, the deposition process can more readily (from an experimental point of view) be biased to feed the interface preferentially from the front or back. This latter situation allows one some control over the mechanism that leads to the meandering instability first analyzed by Bales and Zangwill [1], so that one might hope to

E-mail address: schulze@math.utk.edu.

0022-0248/$ - see front matter © 2006 Elsevier B.V. All rights reserved.
doi:10.1016/j.jcrysgro.2006.07.027

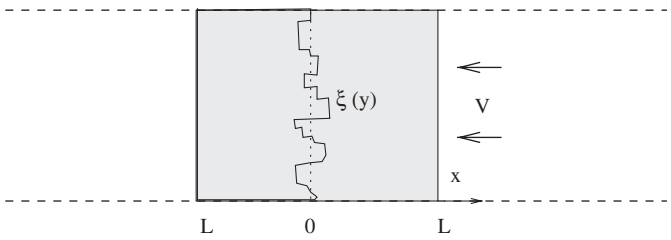

Fig. 1. A schematic diagram of the continuous processing configuration under consideration, showing the substrate motion, stationary deposition zone, mean and actual interface position. The height to the left of the interface is one, to the right zero, so that the step is growing toward the right-hand boundary.

adjust the length scale of any patterns that form naturally for a given material or induce a pattern in a material that does not produce one naturally. As explained further below, this biased deposition process is more complicated for multi-step growth, as it leads to a nonuniform step spacing.

The continuum model developed by Burton et al. [10], provides a well-established tool for examining the macroscale trends of the growth process. Its limitations are well known, in that it is typically used in a deterministic form that yields a mean field result, assumes a continuous curve for the step boundaries, and is aimed at near-equilibrium systems. Nevertheless, these models are viewed as giving important insight into the mechanisms controlling different types of growth morphologies and have been expanded to include many diverse effects (see Ref. [13] for a recent review of epitaxy literature). Our use of the continuum approach will be limited to the linear stability analysis of a single step. Thus, some of the more complicated effects, such as step–step interactions, can be safely avoided. For the flow of a single step comprised of a single species, the possible morphologies are limited to combinations of the following: stable, but rough, front (i.e. step edge), unstable front with fractal structure due to diffusion-limited aggregation [14] and an unstable front with a well-defined length scale giving rise to a fingering instability. It is also possible for islands to nucleate away from the primary front and these may also be unstable. In this paper, parameters, in particular, the domain size L, were selected to ensure that nucleation was extremely rare as it invalidates the analysis based on the continuum model.

To address the fully nonlinear regime and include stochastic effects, we shall turn to kinetic Monte-Carlo (KMC) simulations [15,16]. This method, too, has well-known limitations, including a restricted catalog of events that can miss concerted moves of atoms and severe limitations on the extent to which elastic effects can be accounted for [17]. Despite these drawbacks, KMC gives a much more realistic picture of film growth than the continuum approach. For example, "entropic" step repulsion, i.e. the tendency of steps to maintain some separation due to the fact that they cannot cross one another without producing an overhang, is fully accounted for in this approach.

In Section 2, we briefly review the formulation for both of these methods, emphasizing the boundary conditions that are appropriate for continuous growth. Section 3 discusses results related to the steady-state solutions of the BCF model. Section 4 contains results of a linear stability analysis of the BCF model and in Section 5 we make comparisons of these results with the results of the fully nonlinear and stochastic KMC simulations. The final section summarizes our results and draws some conclusions concerning the relevance of this work to the manufacturing of self-assembled monolayers.

2. Formulation

We consider deposition of a monolayer of material by a beam of intensity $\mathscr{F}(\mathbf{x}) = F + Gx$, where x measures distance in the direction of the step-flow and is restricted to the range $-L<x<L$ in a frame of reference that moves to the right with the mean interface speed V relative to the substrate which is continuously fed into the domain from the right. In contrast to previous studies, we will impose either reflection or absorption boundary conditions at the left and right boundaries $x = \pm L$ along with periodic boundary conditions in the direction parallel to these boundaries.

2.1. KMC simulations

We begin by describing the details of the KMC simulations, which take the form of the typical cube-on-cube growth model with hopping rates in the four lateral directions based on an energy barrier of the form:

$$\Delta E = E_s + nE_n + E_b,$$

where E_s is a substrate contribution to the energy barrier present at every lattice location, E_n is a contribution from each of the lateral nearest neighbors, the number of which can range from zero to four, and E_b is an additional energy barrier

added for ascending/descending moves in order to model the presence of step-edge barriers. While the focus here will be on monolayer growth with negligible nucleation, the simulations allow atoms to cluster and stack or unstack as the film evolves with the convention that only atoms which are on top of the film are allowed to move. This commonly used solid-on-solid convention prevents vacancies and overhanging regions from forming.

In these simulations, the width of the domain in the growth direction, $2L$, is an integer multiple of the lattice spacing a and the "continuous" processing is implemented by shifting the substrate and the atoms on its surface to the left whenever the net deposition onto the substrate is sufficient to produce a net row of growth on each step that is present. As a result, the mean growth actually experiences a small "ratchet" effect which we ignore in the continuum model described below.

Following standard KMC procedures [15,16] atoms hop to neighboring sites with rates given by the Boltzmann factors

$$R = K(T)\exp(-\Delta E/(k_{\mathrm{B}}T)),$$

where T is the temperature, k_{B} is Boltzmann's constant and K is a temperature-dependent constant. We shall adopt the parameter regime used in Ref. [12] for most of our simulations, including the value $K = 2 \times 10^{11}$ Hz. The simulations described below make use of an efficient data structure that allows for quick identification of which event among the typically several million possibilities a uniformly distributed random number corresponds to [18]. The key to this approach is to sort events with the same rates into lists and maintain inverse arrays that coordinate the location of events on the surface with their respective locations within these lists. This approach scales with the number of independent rates, in this case six, rather than with the number of events. While also very efficient, the commonly used binary tree search described in Ref. [19] scales as the logarithm of the number of events and is therefore less efficient than the sorting technique for large simulations. Since our primary focus is on the role of a gradient in the deposition flux rather than the step-edge barrier, the latter effect is implemented in only a small portion of the simulations. When needed, this is done by rejecting an appropriate percentage of moves where adatoms attempt to move from one level of growth to another.

Previous analysis and simulations of step meandering instabilities have made use of "helical" boundary conditions where the adatom field is periodic in both the growth and lateral direction and the lowest step reconnects to the highest step in an Escher stair-case like fashion. For growth onto a continuously supplied substrate and other realistic growth scenarios, these boundary conditions are inappropriate, as they lead to significant in-phase feedback from one end of the domain to the other (see Fig. 4, discussed below). Here, we account for the finite size of the deposition zone by eliminating this feedback mechanism and model the upwind and downwind boundaries as either perfectly reflecting or perfectly absorbing. Still other possibilities include combinations of these fundamental types of boundary conditions that match onto some far-field adatom density derived from the continuum model described below or coupling to the continuum model in a hybrid approach [20,21]. This paper focuses on the pure, homogeneous reflection and absorption conditions with the aim of gaining insight into this entire range of possibilities.

For the reflecting boundary conditions, which are modeled as homogeneous Neumann conditions in the continuum model, one simply sets the rates for moves out of the deposition zone to zero. When the film is moved backward after a net growth of one atomic site along the entire interface, material is transported out of the downwind side of the domain. One option for the upwind boundary during this transient period would be to transport a clean substrate into the deposition zone, but this would add somewhat to the "ratchet" effect inherent in the discrete growth process. Since these effects are absent in the idealized continuum model, a somewhat closer analogy between the two models involves bringing in the same number of adatoms that are typically present at this boundary when a steady state has been reached. In the present work, this is implemented by monitoring the number of atoms at the upwind boundary just prior to the steps motion and adding an equal number of randomly positioned atoms to an adjacent row of "ghost" cites. Thus, one is effectively implementing a discretized Neumann condition in the same way one would when solving the diffusion equation. For the absorbing boundary conditions, which are modeled as homogeneous Dirichlet conditions in the continuum model, adatoms which hop out of the deposition zone are simply removed from the simulation. Note that the shifting of the substrate can be efficiently implemented by "rotating" the map between the surface location in the x-direction and the storage location in arrays that use the corresponding index i for lattice locations. This procedure, which is unnecessary for the helical-type boundary conditions, avoids any need to actually move data when the substrate is shifted.

Another break with past simulations is the imposing of a nonuniform flux $\mathscr{F}(x)$. This becomes a natural possibility to consider when the deposition is constrained to a moving zone that follows the steps and introduces a potentially useful control parameter as the deposition rate and its gradient are readily adjusted independently of the materials being processed, whereas other factors leading to asymmetry in attachment kinetics are inherent to the materials and nonadjustable.

2.2. Continuum model

The BCF continuum model employs a density $\rho(\mathbf{x}, t)$ of adatoms, which correspond to sites with zero lateral nearest neighbors in the KMC simulations. These atoms hop with a rate R_0 that is very fast compared to the rates for atoms with

lateral neighbors. The model takes the form of a diffusion equation with a diffusivity D directly related to R_0 along with boundary conditions, including a condition to determine the location of the moving step boundaries, which, for our purposes, we assume takes the form of a single continuous, differentiable and single-valued curve $x = \xi(y, t)$. The velocity of the interface is then described by the vector $\mathbf{v}_i = (\xi_t, 0)$. In our analysis, the velocity of the solid film relative to our coordinate system is $\mathbf{v}_f = (-V, 0)$, which introduces an advective term into the diffusion equation whenever the pulling speed V is nonzero. We write the governing equations in terms of the pulling speed and the normal velocity of the interface relative to the film $v_{\mathbf{n}} = (\mathbf{v}_i - \mathbf{v}_f) \cdot \hat{\mathbf{n}}$:

$$\rho_t - V\rho_x = D\nabla^2\rho + F + Gx, \tag{1}$$

$$\pm D\hat{\mathbf{n}} \cdot \boldsymbol{\nabla}\rho|_{\pm} \pm v_{\mathbf{n}}\rho|_{\pm} = k_{\pm}[\rho - \rho_{\mathrm{e}} + \Gamma\kappa]_{\pm} \quad \text{at } x = \xi(y, t), \tag{2}$$

$$\rho_a v_{\mathbf{n}} = D[\hat{\mathbf{n}} \cdot \boldsymbol{\nabla}\rho]_{-}^{+} + v_{\mathbf{n}}[\rho]_{-}^{+} - \Lambda\partial_s^2\kappa \quad \text{at } x = \xi(y, t), \tag{3}$$

$$\rho_x = 0 \quad \text{or} \quad \rho = 0 \quad \text{at } x = \pm L. \tag{4}$$

Eq. (2) defines the total flux into the interface from the left and right in terms of attachment parameters $k_{\pm}$ for the upper and lower side of the step, an equilibrium concentration of adatoms ρ_{e} and a correction to this equilibrium that is proportional to a constant Γ times curvature $\kappa(y, t)$, following the model put forward by Bales and Zangwill. In the latter work, a quasi-static approximation is adopted which we postpone until the next section. The density of lattice sites on the surface is represented by ρ_a, so that Eq. (3) enforces conservation of mass at the interface by balancing the growth of the front with the net loss of mass from the surface, adjusted by an edge diffusion term [22] along the interface. As mentioned above, the boundary conditions at the ends of the domain represent either perfect reflection or absorption of adatoms.

For the purposes of our linear stability analysis of the BCF model, it is sufficient to assume the interface position $\xi(y, t)$ is single valued, though this is clearly not true in general. The normal to the interface $x = \xi(y, t)$ is then $\hat{\mathbf{n}} = (1, -\xi_y)/\sqrt{(1 + \xi_y^2)}$, the curvature $\kappa = \xi_{yy}/(1 + \xi_y^2)^{3/2}$ and the normal velocity of the interface relative to the substrate is

$$v_{\mathbf{n}} = \frac{V + \xi_t}{\sqrt{1 + \xi_y^2}}.$$

In the analysis, the edge-diffusion term in Eq. (3) produces somewhat longer wavelength instabilities and was found by Kallunki et al. [12] to give reasonably good agreement with KMC simulations. Note that those authors also considered a model where edge diffusion was heavily preferred over detachment, which is also an event with coordination number one. In our simulations these types of events are equally probable.

To simplify the following analysis, we will employ scalings where lengths are measured in multiples of the lattice constant a, which we take to be the same in all three directions, and time is measured in multiples of the diffusive time scale a^2/D. In these units the constants D and $\rho_a = 1/a^2$ scale out of the problem. Also, adatom density will be measured relative to the equilibrium value of the adatom density ρ_{e}, which represents the expected number of adatoms on a substrate with no flux and no mean interface motion.

Adopting results presented in Ref. [12], the parameters Γ and Λ, now rescaled, are related to the rates in the KMC model by the equations:

$$\Gamma = 2\rho_{\mathrm{e}}\sinh^2\left(\frac{E_{\mathrm{n}}}{4k_{\mathrm{B}}T}\right),$$

where Γ in this paper is the product of the step stiffness and the equilibrium adatom density $\rho_{\mathrm{e}} = \exp(-2E_{\mathrm{N}}/(k_{\mathrm{B}}T))$ and

$$\Lambda = \frac{\Gamma}{2}\exp\left(-\frac{2E_{\mathrm{N}}}{k_{\mathrm{B}}T}\right).$$

When considered, the step-edge barrier is implemented by reducing rates for ascending/descending hops by an additional factor of $\exp(-E_{\mathrm{b}}/k_{\mathrm{B}}T)$, which can be related to the ratio of the step attachment parameters $k_{\pm}$ in the continuum model.

3. Steady states and the quasi-static approximation

Because growth must proceed at extremely small rates for the surface to maintain a coherent morphology, the typical interface velocity will be very small. For this reason it is common to implement the quasi-static approximation where the mean velocity is zero except on the left-hand side of Eq. (3), where it is needed to balance other small quantities. We will make this approximation below, but first we briefly explore steady states of the unapproximated system and make some comparisons to better understand the role of the pulling velocity V.

For there to be a net flux at each point on the surface, the gradient in the deposition must satisfy $|GL| < F$. Within this constraint, the parameters V, F, L and G can be adjusted *independently* to control the growth of a specific material, the properties of which fix the remaining parameters. We shall restrict our interest to steady solutions to Eqs. (1)–(4) that feature a single, flat interface that maintains a mean position of zero. Conservation of mass (3) will then dictate specific values for the pulling velocity $V = V(G, L, F)$. As mentioned earlier, this constraint is maintained in KMC simulation by monitoring the net growth of the interface, a procedure that could be applied to actual experiments as well. If these target velocities are not maintained, conservation of mass and brief experimentation with KMC simulations suggest more complicated steady solutions that feature incomplete layers of growth. This may provide an alternative mechanism for producing patterns on a substrate, but we do not pursue this here.

For steady states satisfying $\xi = 0$, integration across the entire domain combined with the use of (3) gives the mass balance

$$V + [\rho_x]_{-L}^{L} + V[\rho]_{-L}^{L} + 2LF = 0. \tag{5}$$

This is not an independent constraint, but helps understand certain features of the steady solutions. After applying one of the boundary conditions (4) to this equation, either the second or third term vanishes, and we see that the total mass lost at the step is balanced by the mean deposition of new mass and either the difference between the density fed into the system at the left and removed at the right or the mean deposition minus the diffusive losses at both ends of the domain.

In Fig. 2 we plot the relationship between the mean deposition flux F and the pulling velocity needed to maintain the steady state V for both sets of boundary conditions. In the case of the Dirichlet conditions, the quasi-static result is virtually identical to the unapproximated result, but the corresponding results for the Neumann conditions are different at extremely high velocities. While the latter differences would be negligible at normal growth rates and we shall use the quasi-static results below, we note that the origin of the multi-valued pulling rate when viewed as a function of flux is a compression in the diffusive boundary layer ahead of the moving front when the advective term is significant. As a result, the steady states have an asymmetry that feature higher adatom concentrations on the lower terrace even when $G = 0$. When velocities are small, this is a negligible effect and cannot be detected, for example, in Fig. 3, but for extremely large velocities it leads to correspondingly large fluxes of mass across the upwind boundary. Indeed, in the extreme case of $V \to \infty$, the solution corresponds to bringing an already complete monolayer of growth into the "deposition" zone and the mean flux goes to zero in this limit. As expected, much higher fluxes are needed for the Dirichlet boundary conditions to maintain a given velocity, as much of the mass is lost across the far-field boundaries.

We now adopt the quasi-static approximation, which can be viewed as an asymptotic expansion using the mean deposition rate F as a small parameter and considering the solution at times which are large compared to the diffusive time scale a^2/D so that transients in Eq. (1) can be ignored. A consistent solution is obtained in a distinguished limit where the density $\rho \sim O(F)$ and normal velocity $v_{\mathbf{n}} \sim O(F)$ are both small. Note that one can then ignore, to leading order, the entire left-hand side of Eq. (1) and the advective contributions to Eqs. (2) and (3).

In this limit, the two regions of the domain admit the considerably simplified solutions

$$\rho_{\pm} = A_{\pm} + B_{\pm}x - \frac{F}{2}x^2 - \frac{G}{6}x^3 \tag{6}$$

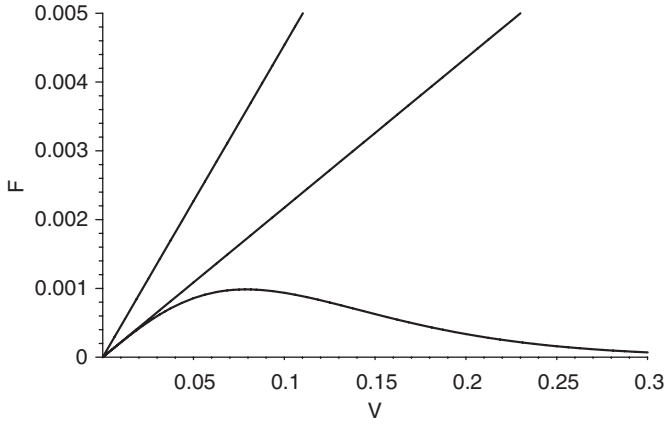

Fig. 2. The flux F required to maintain a steady-state velocity V for the unapproximated system with Neumann boundary conditions (lower curve), the quasi-static approximation of that curve (tangent at the origin) and the corresponding curve for the Dirichlet boundary conditions, which is essentially indistinguishable from the quasi-static approximation for that case.

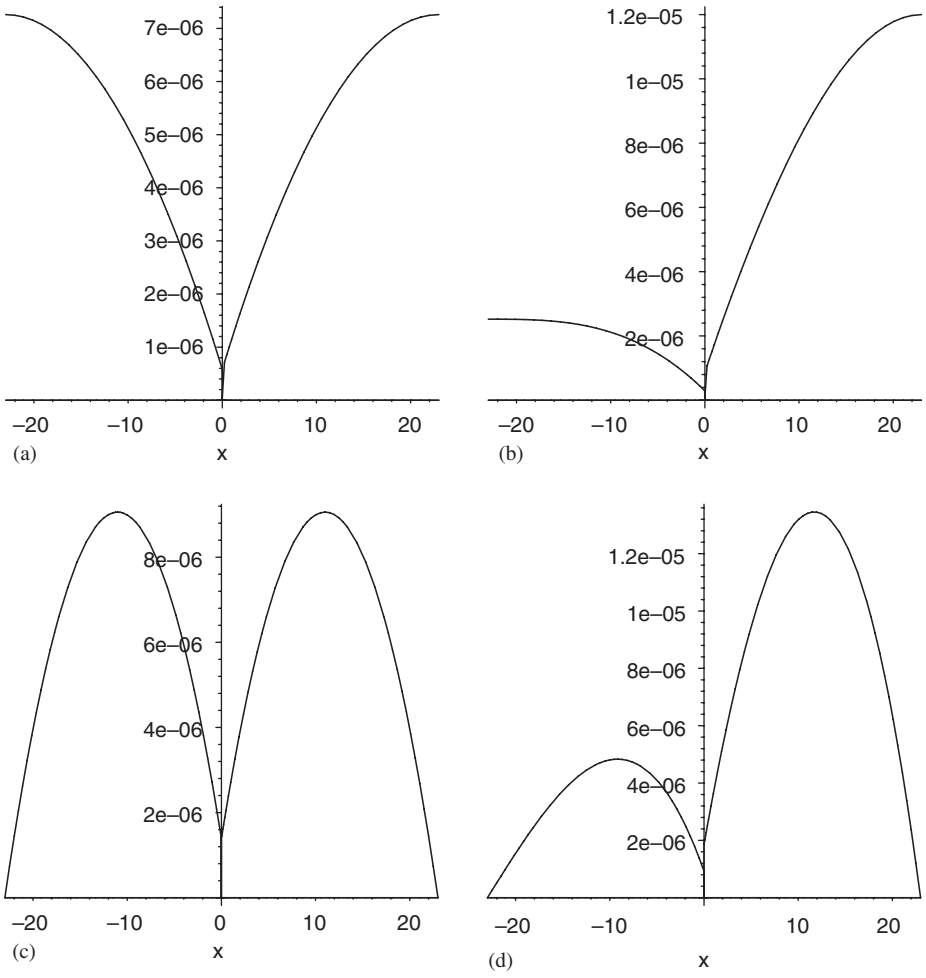

Fig. 3. Profiles of the adatom density of the steady solutions for the Neumann boundary conditions with (a) $GL/F = 0$ and (b) $GL/F = 1$ and the Dirichlet boundary condition with (c) $GL/F = 0$ and (d) $GL/F = 1$. Note the discontinuity at the origin in the asymmetric cases.

and, after applying the boundary conditions (2) and (4) at $x = 0$ we find

$$A_{\pm} = \pm\frac{B_{\pm}}{k_{\pm}}, \tag{7}$$

and either

$$\mp FL - 1/2GL^2 + B_{\pm} = 0, \tag{8}$$

in the case of the Neumann boundary conditions or

$$-\frac{FL^2}{2} \mp \frac{GL^3}{6} + A_{\pm} \pm B_{\pm} = 0, \tag{9}$$

in the case of the Dirichlet boundary conditions.

Finally, applying the conservation of mass condition (3) at $x = 0$ gives, in either case,

$$V = B_{+} - B_{-}. \tag{10}$$

Figs. 4a and b shows typical steady adatom densities for the Neumann boundary conditions with $G = 0$ and $GL/F = 1$, while Figs. 4c and d shows the corresponding adatom densities for the case of Dirichlet boundary conditions.

4. Linear stability analysis

In this section we linearize about the basic state identified above, which we now indicate with an overbar:

$$\rho(x, y, t) = \bar{\rho}(x) + \rho'(x, y, t), \tag{11}$$

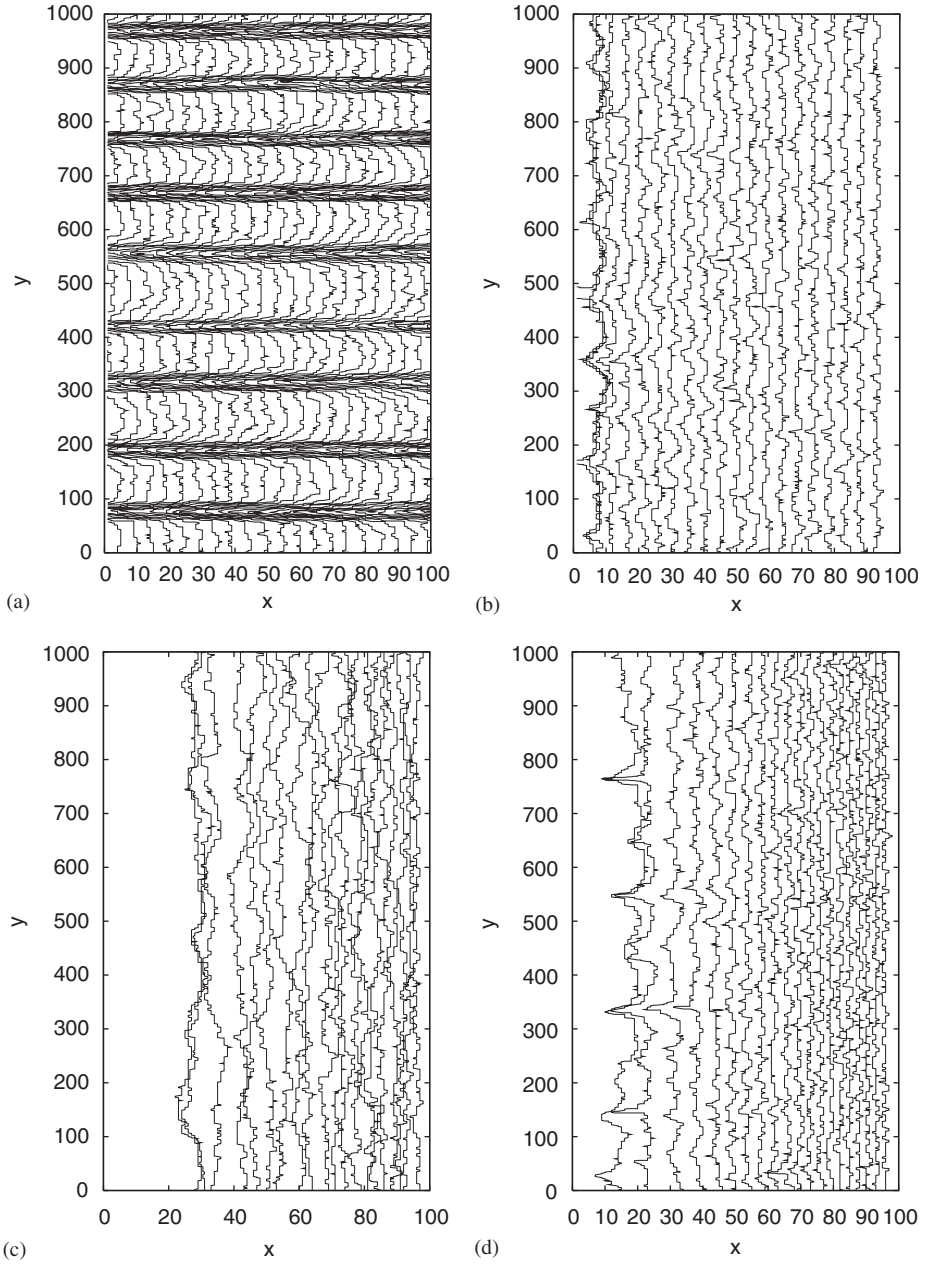

Fig. 4. A train of 20 steps simulated by KMC for 150 monolayers of growth with (a) helical boundary conditions in the horizontal direction, a step-edge barrier of $E_b = 0.15\,\text{eV}$, and no gradient in the deposition flux; (b) reflecting boundary conditions in the horizontal direction, a step-edge barrier of $E_b = 0.15\,\text{eV}$, and no gradient in the deposition flux; (c) reflecting boundary conditions in the horizontal direction, no step-edge barrier and a gradient in the deposition flux such that $GL/F = 1$; (d) reflecting boundary conditions in the horizontal direction, a step-edge barrier of $E_b = 0.15\,\text{eV}$ and a gradient in the deposition flux such that $GL/F = 1$.

$$\xi(y,t) = 0 + \xi'(y,t). \tag{12}$$

The linearized equations and boundary conditions expanded about the leading order interface position are

$$0 = \nabla^2 \rho', \tag{13}$$

$$\pm(\rho'_x + \xi' \bar{\rho}_{xx})|_{\pm} = k_{\pm}(\rho' + \Gamma \xi'_{yy} + \xi' \bar{\rho}_x)_{\pm}, \tag{14}$$

$$\rho'_x|_{\pm L} = 0 \quad \text{or} \quad \rho'_{\pm L} = 0, \tag{15}$$

$$\xi'_t = [(\rho'_x + \xi' \bar{\rho}_{xx}) + V(\rho' + \xi' \bar{\rho}_x)]^+_- - \Lambda \xi'_{yyyy}. \tag{16}$$

We seek the solution of the linearized system in terms of normal modes

$$\rho' = \hat{\rho}(x)\exp(\sigma t + \mathrm{i}\alpha y), \tag{17}$$

$$\xi' = \hat{\xi}\exp(\sigma t + \mathrm{i}\alpha y). \tag{18}$$

This gives rise to the equations

$$0 = \left(\frac{\mathrm{d}^2}{\mathrm{d}x^2} - \alpha^2\right)\hat{\rho}, \tag{19}$$

$$\pm(\hat{\rho}_x + \hat{\xi}\bar{\rho}_{xx})|_{\pm} = k_{\pm}(\hat{\rho} - \alpha^2\Gamma\hat{\xi} + \hat{\xi}\bar{\rho}_x)_{\pm} \quad \text{at } x = 0, \tag{20}$$

$$\hat{\rho}_x|_{\pm L} = 0 \quad \text{or} \quad \hat{\rho}|_{\pm L} = 0, \tag{21}$$

$$\sigma\hat{\xi} = [(\hat{\rho}_x + \hat{\xi}\bar{\rho}_{xx}) + V(\hat{\rho} + \hat{\xi}\bar{\rho}_x)]_-^+ - \Lambda\alpha^4\hat{\xi}. \tag{22}$$

The first of these equations admits solutions of the form

$$\hat{\rho}(x) = \hat{A}_{\pm}\exp(\alpha x) + \hat{B}_{\pm}\exp(-\alpha x). \tag{23}$$

The remaining five equations form a homogeneous system for the five constants $\hat{A}_{\pm}$, $\hat{B}_{\pm}$ and $\hat{\xi}$. In the case of the Neumann boundary conditions, these equations are

$$\begin{bmatrix} \alpha - k_+ & 0 & -\alpha - k_+ & 0 & [\bar{\rho}_{xx} - k_+\bar{\rho}_x + k_+\Gamma\alpha^2]_+ \\ 0 & -\alpha - k_- & 0 & \alpha - k_- & [-\bar{\rho}_{xx} - k_-\bar{\rho}_x + k_-\Gamma\alpha^2]_- \\ \alpha e^{(\alpha L)} & 0 & -\alpha e^{(-\alpha L)} & 0 & 0 \\ 0 & \alpha e^{(-\alpha L)} & 0 & -\alpha e^{(\alpha L)} & 0 \\ \alpha + V & -\alpha - V & -\alpha + V & \alpha - V & -\Lambda\alpha^4 - \sigma \end{bmatrix} \begin{bmatrix} \hat{A}_+ \\ \hat{A}_- \\ \hat{B}_+ \\ \hat{B}_- \\ \hat{\xi} \end{bmatrix} = \mathbf{0}. \tag{24}$$

The corresponding result in the case of the Dirichlet boundary conditions is

$$\begin{bmatrix} \alpha - k_+ & 0 & -\alpha - k_+ & 0 & [\bar{\rho}_{xx} - k_+\bar{\rho}_x + k_+\Gamma\alpha^2]_+ \\ 0 & -\alpha - k_- & 0 & \alpha - k_- & [-\bar{\rho}_{xx} - k_-\bar{\rho}_x + k_-\Gamma\alpha^2]_- \\ e^{(\alpha L)} & 0 & e^{(-\alpha L)} & 0 & 0 \\ 0 & e^{(-\alpha L)} & 0 & e^{(\alpha L)} & 0 \\ \alpha + V & -\alpha - V & -\alpha + V & \alpha - V & -\Lambda\alpha^4 - \sigma \end{bmatrix} \begin{bmatrix} \hat{A}_+ \\ \hat{A}_- \\ \hat{B}_+ \\ \hat{B}_- \\ \hat{\xi} \end{bmatrix} = \mathbf{0}. \tag{25}$$

These homogeneous systems will have a nontrivial solution if they are singular, which yields an unwieldy dispersion relation that we omit. For a given set of parameters $\{F, G, L, \Gamma, \Lambda, k_+, k_-\}$, this gives rise to a unique, real growth rate σ that determines the linear stability of an infinitesimal disturbance with wavenumber α. We discuss the results and give some long-wave approximations for the dispersion relation in the next section. These results were checked by comparing with a numerical result provided by Hausser using the code developed in Ref. [23] and by repeating the calculations for the case with $G = 0$, helical boundary conditions, and a positive step-edge barrier, which allowed direct comparison with the result in Ref. [8].

5. Results

In this section we primarily focus on a comparison between the growth rates predicted by the linear theory in the quasi-static approximation and results obtained from extensive simulation by KMC. We begin, however, by briefly contrasting an important qualitative difference between the continuously processed system and systems of periodic step trains, as revealed by KMC simulation.

In Fig. 4a we show the results of evolving a surface covered by 20 steps in a periodic/helical arrangement in the presence of a step-edge barrier, but no deposition gradient. The mean deposition rate was 0.5 monolayer per second and the figure shows the surface configuration after 300 s of simulated growth. These results, typical of those found by many others, demonstrate a meandering instability with a well-defined wavelength. The remaining parameters are taken from the case considered in Ref. [12], in particular, we have adopted their values of $E_s = 0.35\,\mathrm{eV}$, $E_n = 0.21\,\mathrm{eV}$, $E_b = 0.15\,\mathrm{eV}$ and substrate temperature $T = 375\,\mathrm{K}$. In Fig. 4b we show the result of evolving the same number of steps with the same material parameters for an equal length of time but using reflection boundary conditions at the left and right of the step train rather than the periodic/helical conditions. In this case, we once again see the influence of the step-edge barrier, but

the instability is not so pronounced nor is the wavelength so well-defined. We attribute this to the lack of feedback along the entire step train. This result strongly suggests that the periodic/helical boundary conditions give an unrealistic picture of the extent to which the meandering instability will manifest itself in experiments. In Fig. 4c we trigger the instability using a gradient in the deposition flux such that the mean flux remains the same as in the previous cases but the flux is zero at the left boundary and a maximum at the right boundary. In this figure, the step-edge barrier has been removed, but the rest of the material and control parameters are the same as the first two cases. As indicated earlier, the steady-state solution of the system for multiple steps in the presence of a deposition gradient features nonuniformly spaced steps. As a result, the wavelength of the instability adjusts from longer to shorter waves as you move from left to right in the figure and the resulting pattern is complicated and largely incoherent. In Fig. 4d the instability is due to both the step-edge barrier and a gradient in the deposition flux, with results similar to those of Fig. 4c, although the phase of meanders appears to be better aligned. This suggests that there may be a competing mode of instability where the meanders are out of phase playing a role in Fig. 4c. While these features of the multi-step system are interesting areas for further study, our present aim is to take a closer look at the single-step system that results in monolayer growth.

Turning to the single-step results, in Fig. 5a and b we plot the growth rate σ of infinitesimal disturbances as a function of wavenumber, which we have rescaled so that it reflects the number of wavelengths that can be fit into a width $W = 1000$, which is the domain width used in the KMC simulations. This will facilitate comparison with results of the KMC simulations presented in Figs. 6 and 7. The three curves shown in each figure reflect the three cases $GL/F = 0$, $\frac{1}{2}$ and 1 with the mean flux held constant at $F = 0.5$ for the Neumann conditions and $F = 2.5$ for the Dirichlet conditions. These values were chosen after considerable experimentation so that the driving force for the instability would be strong enough to overcome the substantial noise inherent in the KMC solutions—and presumably the actual physical process—which tends to mask the instability at lower fluxes and lower gradients. At the same time, if one increases the flux too far, one finds that islands begin to form on the surface of the film, rendering the results of the stability analysis meaningless and substantially altering the growth morphology. The different values used for the fluxes for the two cases reflect, in part, the fact that considerable mass is lost across the boundaries for the Dirichlet boundary conditions, but there are also substantial differences, discussed below, in the way the interface responds to the parameter GL/F in the two cases. The remaining parameters, with the exception of the Schwoebel barrier, are the same as in Fig. 4.

As is well known from the analysis of periodic step flows, the system is ill posed when $\Gamma = 0$, in the sense that it loses stability to a mode with infinite wave number, but, for positive Γ, the system is well posed. With $\Gamma > 0$, the system will undergo a meandering instability if there is any mechanism to promote more attachment from the lower step. (For step flow, preferred attachment from the upper step is known to be associated with a step bunching phenomenon which is not relevant to monolayer growth.)

Our remaining results focus on the role of the deposition gradient for monolayer growth in the absence of step-edge barriers. To this end, we use the parameter values $k_- = k_+ = 1$, which, if we recall the scaling that is in force, is equivalent to setting the attachment parameters equal to the adatom hopping rate. For the KMC results, we set the step-edge contribution to the energy barrier to zero. The long-wave approximations to the quasi-static dispersion relations simplify considerably in this case and are given by

$$\sigma \sim L^3 G\alpha^2 - \frac{L^5 G + 6L\Gamma + 3\Lambda + 3L^4 G}{3}\alpha^4 + O(\alpha^6), \tag{26}$$

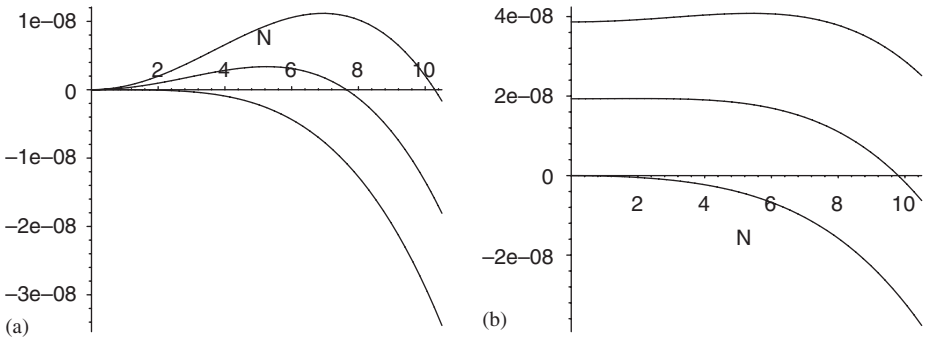

Fig. 5. Plots of the growth rate σ as a function of the wavenumber $N = \alpha W/2\pi$, scaled to the periodic domain width used in the corresponding KMC simulations, for the (a) Neumann boundary conditions and (b) Dirichlet boundary conditions. In each case, the three values of $GL/F = 0$ (lowest curve), $\frac{1}{2}$ and 1 (highest curve) are shown. Note the qualitative change in the Dirichlet case around $GL/F = \frac{1}{2}$, where the fastest growing mode starts to pull away from the origin.

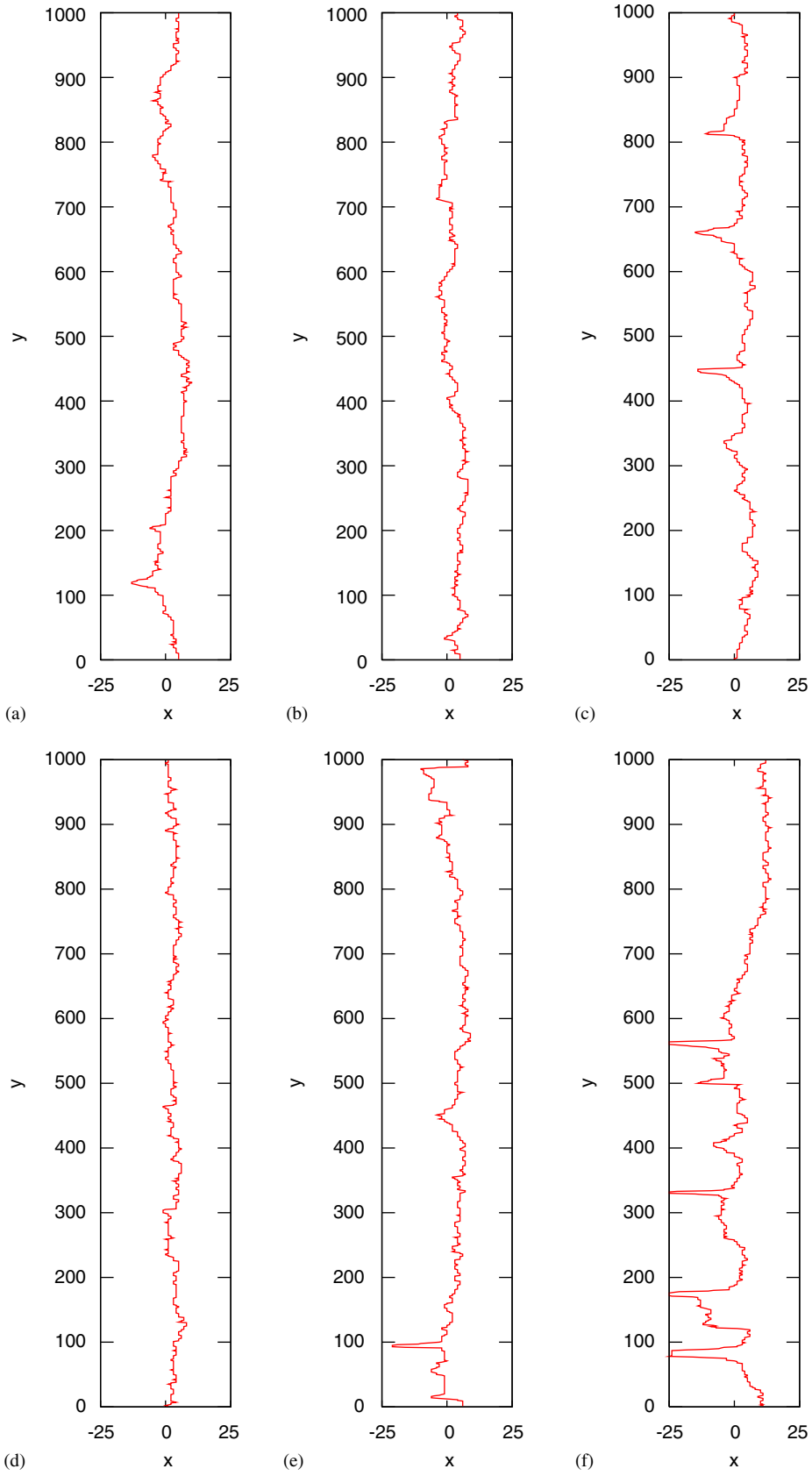

Fig. 6. Snapshots of the interface taken from KMC simulations at arbitrarily chosen but large times for the (a–c) Neumann boundary conditions and (d–f) Dirichlet boundary conditions. Moving from left to right in each case the value of $GL/F = 0, \frac{1}{2}$ and 1, corresponding to the cases considered in Fig. 5.

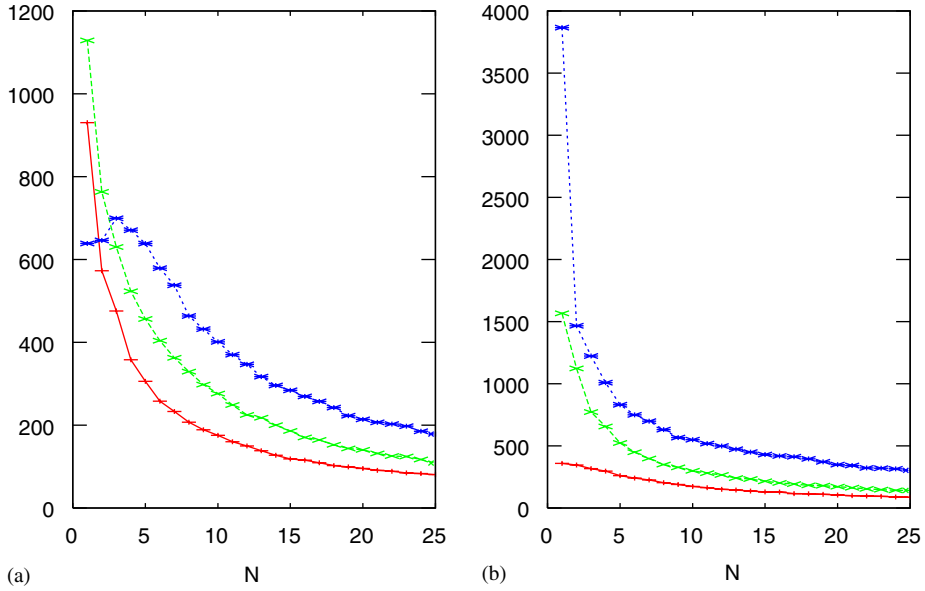

Fig. 7. Plots of the averaged discrete Fourier transforms of the interfacial profiles like those shown in Fig. 6 for (a) Neumann boundary conditions and (b) Dirichlet boundary conditions. The three curves once again correspond to the cases $GL/F = 0$, $\frac{1}{2}$ and 1, moving from the lower to uppermost curve in each case (in the Neumann case the uppermost curves actually cross near the origin; the case $GL/F = 1$ corresponds to the curve with maximum response at mode number three).

for the Neumann boundary conditions and

$$\sigma \sim \frac{L^3 G}{3(L+1)^2} - \frac{-L^6 G + 18L^2\Gamma + 36L\Gamma + 18\Gamma}{9(L+1)^3}\alpha^2 + O(\alpha^4), \tag{27}$$

for the Dirichlet boundary conditions. These results are reflected in Figs. 5a and b, where the numerically evaluated dispersion relation (i.e. no long-wave approximation) is plotted. For the Neumann boundary conditions, there exists growing modes, for sufficiently wide domains, whenever there is any bias, $G>0$, toward depositing more material on the lower terrace. Thus, the critical "morphological" parameter, GL/F, is zero for this case and the instability is a long-wave instability in that it first sets in at zero wavenumber as you pass this threshold. Since the shorter wavelengths are strongly damped by the line tension Γ, the competition between these effects produces a finite wavenumber for the most rapidly growing mode for values of $G>0$. As noted previously, the effect of edge diffusion is to push the instability to somewhat larger wavelengths.

For the Dirichlet case, the critical condition is again $GL/F = 0$ and the instability once again sets in at long wavelengths as this threshold is surpassed, but the instability remains a long-wave instability for sufficiently small, but finite, values of GL/F—i.e. according to the linear theory, there would be a never-ending coarsening process as the system evolved toward longer and longer wavelength patterns in this regime. For finite sized domains, like those used in the KMC simulations, the coarsening continues until the disturbance wavelength is equal to the domain width. As G is increased, with the other parameters held fixed, the influence of the deposition gradient in the second term overcomes the damping effects of the longest waves and the fastest growing mode shifts to a finite wavelength. This transition turns out to have a pronounced effect on the nonlinear evolution, according to the KMC results discussed below. For the Dirichlet case, the effect of edge diffusion is weaker and first comes into play at higher order.

We now turn to results of the KMC simulations by first examining a collection of snapshots of the interface taken well after any initial transient effects have disappeared. Figs. 6a–c are snapshots of simulations with the Neumann boundary conditions and the parameters that correspond to the three graphs in Fig. 5a. Figs. 6d–f are for the Dirichlet case and correspond to Fig. 5b in the same way. In examining these results, it is important to realize that, while there clearly is a transient period of growth, the interface always remains rough and never really approaches anything like a steady state due to the constant presence of stochastic fluctuations. In view of this, a deliberate effort was made to select these snapshots at random, to avoid giving the impression that the coherent patterns with well-defined dominant wavelengths that sometimes form are robust. The stochastic effects are much more pronounced than for the case of a step train with periodic boundary conditions presented in Fig. 4a and discussed in detail in Ref. [12]. The reason for this is that the instability in that case is able to evolve into a strongly nonlinear state with a large amplitude pattern that reinforces itself. In particular, notice that the fingers in fronts shown in Fig. 4a are so deep that they cross the leading edge of several fronts moving behind them. In contrast, both the Dirichlet and Neumann conditions prevent the amplitude from evolving beyond a certain level. As noted previously, it also appears that the periodic boundary conditions in the growth direction introduce a much higher level of alignment in the phase of the meanders than one can expect for more realistic boundary conditions.

The stochastic nature of the results limit somewhat the utility of the linear, or even nonlinear, theory and increases the difficulty of making a direct comparison, but the analysis of the BCF model is still able to correctly predict trends and approximate scales when the instability is driven with sufficient force. Examination of Figs. 6a and b, for example, does not reveal any evidence of a systematic morphological instability, but Fig. 6c, which is forced with the maximum value of $GL/F = 1$, shows evidence for the meandering instability, but no clear value of a preferred wavelength. (Note the three fingers in the upper half of the domain.) A similar statement holds for Figs. 6d–f, only the fingers are deeper, penetrating all the way to the trailing edge of the domain and the instability appears to have been triggered with $GL/F = 0.5$.

To achieve systematic statements, one must follow the system for extremely long periods of time and do extensive averaging. For this we turn to the Fourier spectrum of many snapshots like those shown in Fig. 6. Figs. 7a and b show averages of Fourier coefficients for 1000 samples taken at very long intervals of 10^8 KMC steps to reduce correlations between samples. Thus, these results characterize a single, long simulation, sampled repeatedly. For each sample, the curve $\xi(y, t)$ is resolved into a Fourier series

$$\xi(y,t) = \sum_{N=-\infty}^{\infty} c_N \exp(i2\pi N y/W),$$

where W is the width of the domain, and it is the RMS contributions to each wavelength $\sqrt{c_N^2 + c_{-N}^2}$ that have been averaged over the 1000 samples to produce the graphs. This procedure was chosen over a true ensemble averaging to avoid having to calculate through a lengthy transient period for each sample. The first thing to notice about these graphs, is that even when $GL/F = 0$, there is a tendency of the system to coarsen (i.e. to evolve toward the longest wavelength allowed by the width of the domain). Coarsening is a common feature of stochastically driven systems of this type and all calculations, including many not reported in this manuscript, indicated an underlying coarsening effect that lead to a decaying Fourier spectrum, favoring the longest wavelength in the system. Another effect which may account for some of the long-wave dominance is that the Fourier analysis will identify a front like that appearing in Fig. 6f, where there are several fingers but they are bunched together, as having a dominant single-wavelength component. It was observed, by tracking the same solution over long periods of time that this would sometimes happen even when there had been, say, three persistent fingers for a very long time that were sometimes uniformly spaced and sometimes bunched.

Despite these long-wave biases, Fig. 7a, which corresponds to the Neumann case, reinforces the impressions gleaned from the snapshots in Fig. 6, in that the morphological instability induced by the gradient in the deposition flux is clearly present in the data for the $GL/F = 1$ case. Comparing this figure with Fig. 5a, we see that a three-wavelength response was statistically dominant, whereas the linear theory indicates that mode seven would have grown the fastest for an infinitesimal disturbance. In all of the calculations that were performed, including those not presented, the dominant wavelength was as long (in single-wavelength situations) or longer than the fastest growing infinitesimal wave. This could be due to a nonlinear effect, the stochastic coarsening mechanism just mentioned or a combination of these. Also, from the results of Ref. [12], one would expect the linear theory to have some error even in the much more predictable periodic case. Finally, notice that there is clear evidence that the gradient in the deposition flux has triggered an increase in the amplitude of the interfacial disturbances for the Neumann case even at smaller values of GL/F, like the intermediate case presented in Fig. 7b. Additional intermediate cases not shown showed a systematic increase in the strength of the lower Fourier modes as G was increased, with a gradual shift to a higher mode response for the largest values of G.

Turning to the Dirichlet data, Fig. 7, like Fig. 6, reveals a qualitative difference from the Neumann case, in that a multiwavelength response was never favored once transients had died away, despite considerable effort to find parameters for which it would be. Instead, the simulations revealed that at some critical value of G, either a single deep finger or a group of deep fingers that were bunched together was always found to give a the Fourier spectrum with a dominant mode-one response. The triggering of this transition, which was suggestive of a nonlinear jump bifurcation, appeared to coincide with the shift of the dominate wavelength in Fig. 5b away from a zero wavenumber response. The transition to this type of behavior is reflected in Fig. 7b by an extremely large mode-one response that distorts what appears to be an otherwise exponentially decaying spectrum.

Finally, it was observed that the evolution of the system wavelength, to the extent that one could be identified, would at times lock onto a particular mode for rather long intervals before jumping to another mode or entering an interval over which there was no clear response. Observing the systems behavior for too short a period of time could therefore lead to the mistaken conclusion that a particular mode was consistently dominant.

6. Conclusions

In this paper we used both KMC and the mean field BCF model to examine the continuous coating of a crystalline substrate by a single monolayer of epitaxial film. Our aim was to explore the possibility of inducing and controlling an interfacial meandering instability using the gradient of the deposition flux. Control of the interfacial morphology in the

single species context considered here would be primarily of scientific interest. If this could be accomplished in a robust manner, however, it is possible that the meanders that form could be exploited to guide the nucleation and growth of a second species, for example, so that nanowires could be embedded within the film or that some similar nanotexturing could be accomplished.

An important aspect of using the deposition flux to control the morphology is that the gradient in the flux can be adjusted independent of the material parameters. Establishing a significant gradient over such a small length scale in an experiment or manufacturing process might prove challenging. Note that this flux, as a function of the coordinate in the growth direction $\mathscr{F}(x)$, need not be strictly linear, as the mechanism of the instability would be present as long as we have $\mathscr{F}'>0$. We must keep in mind that this flux takes the form of a stochastic process, as in the KMC simulations, rather than the deterministic function of the mean field theory. Such a process could be established in a variety of ways. For example, two independent sources of particles with different intensities placed at some distance from one another or a single source screened by one or more nanoscale obstacles would be sufficient. One could also manipulate the process with some external forcing like a magnetic field or a flow-field in a vapor-deposition process.

The mechanism under consideration may be best suited to monolayer growth, as a gradient in the deposition flux would produce uneven step spacing in multistep coatings. In any event, this uneven spacing complicates the analysis, which has been limited to the single-step case in the present study. Aside from the gradient in the deposition flux, the most significant departure from previous studies is the consideration of Neumann and Dirichlet boundary conditions in place of the helical boundary conditions used to analyze the evolution of periodic step trains on miscut surfaces. These alternatives provide more realistic descriptions of the processing geometry under consideration and significantly alter the behavior of the system as they prevent the feedback mechanism from step to step that reinforces the interfacial pattern in step flow. Indeed, the principal observation from the KMC study was that this resulted in a highly fluctuating interfacial instability, with a wavelength that was often ill defined and only capable of sustaining a coherent wavelength for a limited period of time. To make meaningful contact with the linear mean-field theory, it was necessary to average the KMC data over very long periods of time.

An interesting contrast between the two types of boundary conditions considered was the tendency of the Dirichlet model to jump to a single mode response (i.e. a dominant wavelength equal to the width of the domain) when the deposition gradient was increased sufficiently. This appeared to coincide with a qualitative change in the fastest growing wavelength *away* from the long-wave limit. We offer here a possible mechanism that might account for this result. As the deposition gradient is increased into the regime where the linear theory predicts a finite value for the wavelength of the fastest growing mode and this mode becomes small enough to fit within the periodic domain that is being simulated, a significant interfacial disturbance at this wavelength begins to form during a transient growth period. It is natural that the preferred wavelength of this disturbance will change with the increasing amplitude as a result of nonlinear effects for either type of boundary conditions, and it appears, from the KMC simulations, that this favors longer wavelength disturbances in this system. In the case of the Dirichlet boundary conditions, the trailing regions of the front—which take the form of fingers—eventually grow into a region that is increasingly depleted of adatoms, and the finger formation process is then greatly enhanced. This appears to be the mechanism that triggers a transition to a larger amplitude response, which would then be associated with a corresponding jump to larger wavelengths. These observations lead to a number of interesting issues that might be explored by means of a nonlinear study of the mean field model and the study of a stochastic version of that theory.

Finally, one has to conclude from the KMC simulations that the meandering instability induced by a fixed deposition gradient cannot be relied upon to maintain a robust interfacial pattern. Future efforts to explore this mechanism might consider active control of the deposition gradient, which could, to some extent, provide a feedback mechanism that might stabilize the preferred mode with respect to the stochastic fluctuations.

Acknowledgments

The author would like to thank D.M. Anderson, F. Hausser and A. Voigt for suggestions that improved an earlier draft of this manuscript. A special thanks to F. Hausser for performing some numerical calculations to validate the results of the linear stability analysis. Finally, thanks to the Department of Energy for supporting this research via Grant no. DE-FG02-03ER2558.

References

[1] G.S. Bales, A. Zangwill, Morphological instability of a terrace edge during step-flow growth, Phys. Rev. B 41 (1990) 5500.
[2] R.L. Schwoebel, E.J. Shipsey, Step motion on crystal surfaces, J. Appl. Phys. 37 (1966) 3682.
[3] R.L. Schwoebel, Step motion on crystal surfaces 2, J. Appl. Phys. 40 (1969) 614.
[4] G. Ehrlich, F. Hudda, Atomic view of surface diffusion: tungsten on tungsten, J. Chem. Phys. 44 (1966) 1039.

[5] S.H. Davis, Theory of Solidification, Cambridge University Press, Cambridge, 2001.
[6] S. Donet, F. Weiss, P. Chaudouet, S. Beauquis, A. Abrutis, H.C. Freyhardt, A. Usokin, D. Selbmann, J. Eickemeyer, C. Jimenez, C.E. Bruzek, J.M. Saugrain, Reel-to-reel MOCVD for YBCO coated conductor, IEEE Trans. Appl. Superconductivity 13 (2) (2003) 2524.
[7] R.E. Caflisch, B. Li, Analysis of island dynamics in epitaxial growth of thin films, Multiscale Model. Simul. 1 (2003) 150.
[8] F. Gillet, O. Pierre-Louis, C. Misbah, Non-linear evolution of step meander during growth of a vicinal surface with no desorption, Eur. Phys. J. B 18 (2000) 519.
[9] A. Pimpinelli, I. Elkinani, A. Karma, C. Misbah, J. Villain, Step motions on high-temperature vicinal surfaces, J. Phys. Condens. Matter 6 (1994) 2661.
[10] W.K. Burton, N. Cabrera, F.C. Frank, The growth of crystals and the equilibrium structure of their surfaces, Phil. Trans. R. Soc. London 243A (1951) 299.
[11] M. Rost, P. Smilauer, J. Krug, Unstable epitaxy on vicinal surfaces, Surface Sci. 369 (1996) 393.
[12] J. Kallunki, J. Krug, M. Kotrla, Competing mechanisms for step meandering in unstable growth, Phys. Rev. B 65 (2002) 205411.
[13] J.W. Evans, P.A. Thiel, M.C. Bartelt, Morphological evolution during epitaxial thin film growth: 2D islands and 3D mounds, Surface Sci. Rep. 61 (2006) 1.
[14] T.A. Witten, L.M. Sander, Phys. Rev. Lett. 47 (1981) 1400.
[15] A.B. Bortz, M.H. Kalos, J.L. Lebowitz, New algorithm for Monte-Carlo simulation of Ising spin systems, J. Comput. Phys. 17 (1975) 10.
[16] M. Kotrla, Numerical simulations in the theory of crystal growth, Comp. Phys. Comm. 97 (1996) 82.
[17] A.F. Voter, Introduction to the kinetic Monte Carlo method, in: Radiation Effects in Solids, Proceedings of the NATO Advanced Study Institute on Radiation Effects in Solids, Springer, Berlin, 2006.
[18] T.P. Schulze, Kinetic Monte-Carlo simulations with minimal searching, Phys. Rev. E 65 (2002) 36704.
[19] J.L. Blue, I. Beichl, F. Sullivan, Faster Monte-Carlo simulations, Phys. Rev. E 51 (1995) 867.
[20] T.P. Schulze, P. Smereka, W. E, Coupling, Kinetic Monte-Carlo and continuum models with application to epitaxial growth, J. Comp. Phys. 189 (2003) 197.
[21] T.P. Schulze, A hybrid method for simulating epitaxial growth, J. Crystal Growth 263 (2004) 605.
[22] T. Ihle, C. Misbah, O. Pierre-Louis, Equilibrium step dynamics on vicinal surfaces revisited, Phys. Rev. B 58 (1998) 2289.
[23] E. Bansch, F. Hausser, O. Lakkis, B. Li, A. Voigt, Finite element method for epitaxial growth with attachment–detachment kinetics, J. Comp. Phys. 194 (2004) 409.